Nanoscale

PAPER

View Article Online
View Journal | View Issue

Cite this: *Nanoscale*, 2025, **17**, 1497

A layered Janus metastructure for multi-physical quantity detection based on the second harmonic wave†

Yu-Xin Wei, Jun-Yang Sui, Chuan-Qi Wu, Chu-Ming Guo, Xiang Li and Hai-Feng Zhang *

In the field of nonlinear optics and physical quantity detection, the use of the second harmonic wave (SHW) generated in ferroelectric crystals is proposed to realize multi-physical quantity detection with the Janus property. In view of the single physical quantity detected by the current research and the single application scenario, this paper proposes a multi-functional and novel nonlinear Janus metastructure (NJMS), which exploits the SHW to achieve highly sensitive multi-physical quantity detection in the terahertz frequency range and shows Janus properties in both the forward and backward directions of the system. The NJMS is realized to detect refractive indices, thicknesses, and angles with different modes in the forward and backward directions. The proposed NJMS broadens the application scenario of the SHW and provides a novel idea for the research of multi-physical quantity detection devices with the Janus property.

Received 13th August 2024,
Accepted 22nd November 2024

DOI: 10.1039/d4nr03341h

rsc.li/nanoscale

1. Introduction

Early studies on microwave and radio frequency have demonstrated that nonlinear phenomena occur when the electric field is very high.[1] This is because when the electric field interacts with the material, if the electric field is very low, the nonlinear term in the expression for the polarized dipole moment can be neglected.[1] The dipole produced is proportional to the electric field, that is, a linear effect. When the electric field is very high, the nonlinear term can no longer be ignored, and thus, phenomena such as quadratic frequency doubling and frequency mixing can be generated.[1] The emergence of nonlinear optical phenomena has revolutionized the landscape of the optical field, forcing us to study them in depth.

The second harmonic wave (SHW), a frequency doubling process, is a second-order nonlinear optical effect.[2–4] When a beam of electromagnetic waves (EWs)[5] with a frequency of ω, the fundamental wave (FW), is incident on a material with second-order nonlinear optical properties, it induces a change in the charge distribution in the medium, which in turn produces polarization. This polarization produces components with the same frequency as the incident EWs and components with twice the frequency of the incident EWs, which is the SHW.[6] When these polarized waves interfere with each other and satisfy specific phase-matching conditions,[7] EWs with a frequency of 2ω are radiated. The efficiency of second harmonic generation is mainly affected by the nonlinear magnetization index of the material itself,[8] the intensity of the incident EWs,[9] and the phase matching.[10] Due to the inherent nonlinear magnetization index of the material and the limitation of the intensity of the incident EWs, the critical factor in determining the output efficiency of the strong SHW depends on the phase matching between the SHW and the FW.[11] Second harmonic generation is the most prevalent among the various nonlinear optical processes. It has great potential in applications that are widely used in fields such as detection,[12] biomedicine,[13] and spectroscopy.[14] For instance, Iida *et al.* proposed an optical frequency-domain optical angle measurement method based on the SHW of a mode-locked femtosecond laser source, achieving a measurable range of 10 000 arc-sec.[15] Sounas *et al.* proposed an impedance-variable SHW sensor consisting of copper wires sandwiched between common-base amorphous ribbons and obtained a maximum voltage variation of the second harmonic of 151.0% per Oe.[16] These SHW electromagnetic sensors exhibit significant advantages in providing real-time and high-sensitivity detection. Thus, the SHW has excellent potential in physical quantity detection and communication. The Janus property is that EWs exhibit different properties when incident in the forward and backward directions.[17] The Janus property can be realized by breaking the

College of Electronic and Optical Engineering and College of Flexible Electronics (Future Technology), Nanjing University of Posts and Telecommunications, Nanjing, 210023, China. E-mail: hanlor@njupt.edu.cn, hanlor@163.com

† Electronic supplementary information (ESI) available. See DOI: https://doi.org/10.1039/d4nr03341h

spatial symmetry of the structure, and the application scenarios of sensors with properties are richer,[17] so the application of properties in sensors has become the focus of current studies. For instance, Li *et al.* proposed a miniaturized, low-cost, high-sensitivity Janus microwave sensor for noninvasive glucose monitoring, and the proposed sensor has a repeatability error of about ±0.2 MHz and ±0.5° in specific cases.[18] This implies a broader detection range and application scenarios for the sensor. Although the current studies have been more perfect, in general, there still does not have the Janus property of the defects.

To make up for the shortcomings of the current research, a multilayer metastructure that introduces nonlinear materials is proposed, which aims to utilize the SHW, a nonlinear optical phenomenon, to achieve the detection of a wide range of physical quantities. By designing a multilayer structure with the introduction of the nonlinear medium strontium barium niobate (SBN),[18] frequency doubling of electromagnetic radiation at fundamental wave incidence and high-precision sensing in the frequency range of the SHW are realized. Since the nonlinear medium in the multilayer metastructure breaks the spatial inversion symmetry, it exhibits the Janus properties in the forward and backward directions of the system. This study provides new ideas for the application of the nonlinear optical phenomenon, which is an innovative combination of multi-physical quantity detection and Janus properties.

2. Configuration and methods

2.1. Structural composition and RI modulation

The composition method of the novel nonlinear Janus metastructure (NJMS) is the key to realizing the sensing function, and this section describes in detail the construction method of the NJMS as well as the calculation of the refractive index (RI) of each layer of material. The structural composition and the construction method of the NJMS are shown in Fig. 1,

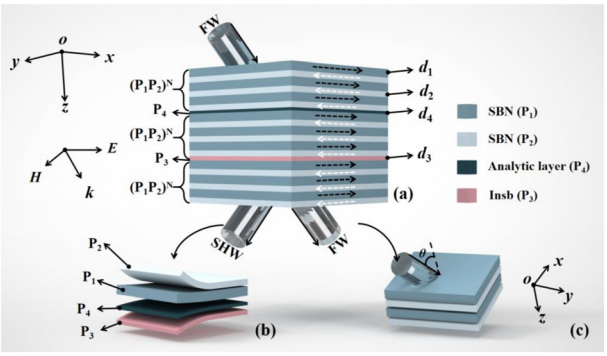

Fig. 1 Structural composition of the NJMS. (a) The overall structure of the NJMS can be described as $(P_1\ P_2)^N\ P_4(P_1\ P_2)^N\ P_3(P_1\ P_2)^N$, the two polarities of the SBN are denoted as P_1 and P_2, and the InSb is denoted as P_2, and the detection layer is denoted as P_4. (b) The thicknesses of P_1, P_2, P_3, and P_4 are d_1, d_2, d_3, and d_4, respectively. (c) The angle of the direction of the perpendicularly incident EWs in the electron-controlled birefringence effect to that of the electric field direction is θ.

where the ambient temperature is 300 K. The magnetic field component of the incident EWs is oriented along the +*y*-axis, while the electric field is parallel to the +*x*-axis. In Fig. 1(a), the NJMS is a quasi-periodic structure composed of SBN with different polarities (P_1 and P_2), indium antimonide (InSb) (denoted as P_3), and a detection layer (denoted as P_4), which can be described in general as $(P_1\ P_2)^N\ P_4(P_1\ P_2)^N\ P_3(P_1\ P_2)^N$, where $N = 4$ denotes the number of periods. Arrows in the layers of P_1 and P_2 denote the direction of polarization of the SBN. In Fig. 1(b), the thicknesses of P_1, P_2, P_3, and P_4 are d_1 = 3.1 μm, d_2 = 2.1 μm, d_3 = 1.93 μm, and d_4 = 1.45 μm, respectively. In Fig. 1(c), it is depicted that the angle between the direction of perpendicular incidence of EWs in the electrically controlled birefringence effect and the direction of the electric field is θ.

The manufacturing process of the proposed structure can be briefly described as follows: SBN can be prepared through metal alkoxides,[19] InSb can be obtained *via* synthetic media,[20] and the detection layer is considered as an ordinary material. After arranging the materials, the NJMS can be obtained through the preparation of layered structures[21] (details can be found in the ESI†). The NJMS can be used to detect the angle θ, the RI of the detector layer (P_4), the thickness, and the forward and backward directions of different modes of detection.

The second-order nonlinear coefficients of each material layer are denoted as $\chi_1^{(2)}$, $\chi_2^{(2)}$, $\chi_3^{(2)}$ and $\chi_4^{(2)}$. The second-order nonlinear coefficients of P_4 are zero since P_4 is assumed to be an ordinary dielectric with almost no nonlinear effects. The SBN exhibits significant nonlinear coefficients of $\chi_2^{(2)}$ = 27.2 pm V^{-1}.[22] As shown in Fig. 1(a), the arrows in the P_1 and P_2 layers indicate that the polarization of the SBN is in opposite directions, and their nonlinear coefficients have a relationship of $\chi_1^{(2)} = -\chi_2^{(2)}$. According to the dispersion equation:[6]

$$n^2 = A_0 + \frac{B_0}{\lambda^2 - {C_0}^2} - D_0\lambda^2. \quad (1)$$

The RI of SBN can be obtained, where A_0 = 5.065, B_0 = 11.13 × 10^4, C_0 = 6.7525 × 10^4, and D_0 = 1.605 × 10^{-5}.[23] The periodically polarized SBN is modulated by the nonlinear magnetization index.[23] The two dielectric layers, P_1 and P_2, are polarized in opposite directions, and their respective refractive indices are expressed as follows:[22]

$$n_1 = n + \Delta n_1 = n + \frac{1}{2}{n_0}^3 r_{33}E, \quad (2)$$

$$n_2 = n + \Delta n_2 = n + \frac{1}{2}{n_0}^3 r_{33}E, \quad (3)$$

where r_{33} is the electro-optical coefficient of the material and E is the electric field amplitude. Thus the refractive indices of P_1 and P_2 under the FW and SHW were calculated as $n_1^{(f)}$ = 1.6096, $n_1^{(s)}$ = 2.8624, $n_2^{(f)}$ = 1.6114, and $n_2^{(s)}$ = 2.8843, respectively. When the EWs propagate in the NJMS, the Lorentz force affects the transverse magnetic (TM) polarized EWs but has no effect on the transverse electric (TE) polarized EWs.[24] The mag-

netic field component of the incident EWs is oriented along the +*y*-axis, while the electric field is parallel to the +*x*-axis. Thus, the effect of the external magnetic field on the TM-polarized EWs is controlled. Therefore, the focus of this study is on the magnetic control performance under TM polarization conditions. When a magnetic field is applied to the NJMS, the dielectric constant of magnetized InSb can be expressed as:[25]

$$\varepsilon_{\mathrm{InSb}} = \begin{bmatrix} \varepsilon_x & 0 & i\varepsilon_{xz} \\ 0 & \varepsilon_y & 0 \\ -i\varepsilon_{xz} & 0 & \varepsilon_x \end{bmatrix}, \tag{4}$$

where i denotes an imaginary number. The components of the tensor are shown below:[25]

$$\varepsilon_x = \varepsilon_\infty - \varepsilon_\infty \frac{{\omega_\mathrm{p}}^2(\omega + i\nu_\mathrm{c})}{\omega[(\omega + i\nu_\mathrm{c})^2 - {\omega_\mathrm{c}}^2]}, \tag{5a}$$

$$\varepsilon_y = \varepsilon_\infty - \varepsilon_\infty \frac{{\omega_\mathrm{p}}^2}{\omega(\omega + i\nu_\mathrm{c})}, \tag{5b}$$

$$\varepsilon_{xz} = -\varepsilon_\infty \frac{{\omega_\mathrm{p}}^2\omega_\mathrm{c}}{\omega[(\omega + i\nu_\mathrm{c})^2 - {\omega_\mathrm{c}}^2]}, \tag{5c}$$

where $\varepsilon_\infty = 15.68$ is the high-frequency limit permittivity of the carriers, $\omega_\mathrm{p} = (n_\mathrm{p}e^2/\varepsilon_0 m^*)^{1/2}$ is the plasma frequency, n_p is the intrinsic carrier concentration, e is the elementary charge, ε_0 is the vacuum permittivity, and m^* is the effective mass of the carriers. $\nu_\mathrm{c} = 8 \times 10^{-6}\omega_\mathrm{p}$ is the plasma collision frequency,[26] and ω is the angular frequency of the FW and the SHW.[26] $\omega_\mathrm{c} = eB/m^*$ is the cyclotron frequency of electrons, and the electron cyclotron frequency is proportional to the applied magnetic field strength B. For InSb, $m^* = 0.015m_\mathrm{e}$, where m_e is the electron mass.[26] The dielectric properties of InSb are closely related to n_p, T denotes the ambient temperature, and n_p can be expressed as:[26]

$$n_\mathrm{p}(\mathrm{m}^{-3}) = 5.76 \times 10^{20} T^{1.5} \mathrm{e}^{-0.26/(2\times 8.625\times 10^{-5}\times T)}. \tag{6}$$

Therefore, the RI of magnetized InSb can be expressed as $n_{\mathrm{InSb}} = (\varepsilon_{\mathrm{InSb}})^{1/2}$, where $\varepsilon_{\mathrm{InSb}} = ({\varepsilon_x}^2 - {\varepsilon_{xz}}^2)/\varepsilon_x$.[26]

2.2. Amplitudes of the FW and SHW

Analyzing the electric field of the FW within the NJMS is the key to determining the transmittance, and in this section, the propagation equation of EWs in a nonlinear medium is derived from the interaction between the FW and the nonlinear medium. For the SHW generated by the interaction with the FW and nonlinear medium, the nonlinear relationship between the polarization strength P and the electric field strength E can be expressed as:[3]

$$P = \varepsilon_0 \chi^{(1)} \cdot E + P_{\mathrm{NL}}, \tag{7}$$

where P_{NL} is the nonlinear component. Substituting Maxwell's equations and nonlinear material equations into eqn (8a)–(8c):[3]

$$\nabla \times \boldsymbol{E} = -\mu_0 \frac{\partial \boldsymbol{H}}{\partial t}, \tag{8a}$$

$$\nabla \times \boldsymbol{H} = \frac{\partial \boldsymbol{D}}{\partial t} + \sigma_0 \boldsymbol{E}, \tag{8b}$$

$$\boldsymbol{D} = \varepsilon \cdot \boldsymbol{E} + P_{\mathrm{NL}}, \tag{8c}$$

where μ_0 is the vacuum magnetic permeability, σ_0 is the vacuum electric permeability, and $\varepsilon = \varepsilon_0[1 + \chi^{(1)}]$, to obtain the following propagation equation of EWs in nonlinear materials:

$$\nabla \times \nabla \times \boldsymbol{E} + \mu_0\sigma_0 \frac{\partial \boldsymbol{E}}{\partial t} + \mu_0 \frac{\partial^2 \varepsilon \cdot \boldsymbol{E}}{\partial t^2} = -\mu_0 \frac{\partial^2 P_{\mathrm{NL}}}{\partial t^2}. \tag{9}$$

Assume that the medium is lossless, that is, $\sigma_0 = 0$. Assume that the nonlinear medium is homogeneous, non-absorbing, and isotropic, that is, $E = 0$, such that $n = (\varepsilon/\varepsilon_0)^{1/2}$, which can therefore be derived from eqn (9):[3]

$$\nabla^2 \boldsymbol{E} - \frac{n^2}{c^2}\frac{\partial^2}{\partial t^2}\boldsymbol{E} = \mu_0 \frac{\partial^2}{\partial t^2} P_{\mathrm{NL}}. \tag{10}$$

Thus, the propagation equations in the FW and SHW forms can be written as:[3]

$$\nabla^2(E^{(\mathrm{f})}) - \frac{\varepsilon^{(\mathrm{f})}}{\varepsilon_0 c^2} E^{(\mathrm{f})} = \mu_0 \frac{\partial^2}{\partial t^2} P_{\mathrm{NL}}^{(\mathrm{f})}, \tag{10a}$$

$$\nabla^2(E^{(\mathrm{s})}) - \frac{\varepsilon^{(\mathrm{s})}}{\varepsilon_0 c^2} E^{(\mathrm{s})} = \mu_0 \frac{\partial^2}{\partial t^2} P_{\mathrm{NL}}^{(\mathrm{s})}, \tag{10b}$$

where $\varepsilon^{(\mathrm{f})}$ and $\varepsilon^{(\mathrm{s})}$ denote the permittivity at the FW and SHW, respectively. $P_{\mathrm{NL}}^{(\mathrm{f})}$ and $P_{\mathrm{NL}}^{(\mathrm{s})}$ represent the nonlinear polarizability at the FW and SHW. c is the magnitude of the propagation velocity of EWs in a vacuum. It is found from the calculation that the electric field of FWs in each layer of the medium when FWs propagate along the +*z*-axis within the NJMS can be expressed as:[3]

$$E_\lambda^{(\mathrm{f})}(z) = E_\lambda^{(\mathrm{f})+} \mathrm{e}^{i[k_{z\alpha}{}^{(\mathrm{f})}(z_0 - z_{\lambda-1}) - \omega t]} + E_\lambda^{(\mathrm{f})-} \mathrm{e}^{-i[k_{z\alpha}^{(\mathrm{f})}(z_0 - z_{\lambda-1}) - \omega t]}, \tag{11}$$

where $E_\lambda^{(\mathrm{f})+}$ and $E_\lambda^{(\mathrm{f})-}$ are the amplitudes of the complex electric field in the positive and negative FWs, respectively. $z_0 = 0$, $z_\lambda = z_{\lambda+1} - d_\lambda$, and $k_{z\alpha}^{(\mathrm{f})}$ are the components of the wave vector of the FW propagating along the z-direction in the medium and satisfies $k_{z\alpha}^{(\mathrm{f})} = n_\alpha^{(\mathrm{f})} k_\mathrm{f} \cos(X_\alpha^{(\mathrm{f})})$, $X_\alpha^{(\mathrm{f})} = \arcsin(n_0 \sin\theta/n_\alpha^{(\mathrm{f})})$, and $k_\mathrm{f} = \omega/c$, ($\alpha = 1, 2, 3, 4$). In each layer of the medium, the magnetic field consists of a combination of transmitted and reflected waves, which can be expressed as:[27]

$$H(x,z) = {H_0}^+ \mathrm{e}^{i\left(k_{x\alpha}^{(\mathrm{f})} x + k_{z\alpha}^{(\mathrm{f})} z\right)} + {H_0}^- \mathrm{e}^{i\left(k_{x\alpha}^{(\mathrm{f})} x - k_{z\alpha}^{(\mathrm{f})} z\right)} = H^+ + H^-, \tag{12}$$

where $k_{x\alpha}^{(\mathrm{f})}$ is the component of the wave vector of the FW propagating in the +*z*-axis in the medium, which remains constant as it propagates through the multilayer structure. $k_{x\alpha}^{(\mathrm{f})}$ and $k_{z\alpha}^{(\mathrm{f})}$ are satisfied between them:[27]

$$k_{x\alpha}^{(\mathrm{f})2} = \frac{\omega^2}{c^2}\frac{{\varepsilon_x}^2 - {\varepsilon_{xz}}^2}{\varepsilon_x} - k_{z\alpha}^{(\mathrm{f})2}. \tag{13}$$

According to Maxwell's curl equations for the magnetic field:[27]

$$\frac{\partial}{\partial z}H_y = i\omega\varepsilon_x\varepsilon_0 E_x + \omega\varepsilon_0\varepsilon_x E_z. \tag{14}$$

The tangential component of the electric field can be calculated from eqn (12) and (13) as:

$$E_x(x,z) = \left(\frac{ik_x\varepsilon_{xz}}{\varepsilon_0\varepsilon_x\varepsilon_{TM}} + \frac{k_z}{\varepsilon_0\varepsilon_{TM}}\right)H_y{}^{+} + \left(\frac{ik_x\varepsilon_{xz}}{\varepsilon_0\varepsilon_x\varepsilon_{TM}} - \frac{k_z}{\varepsilon_0\varepsilon_{TM}}\right)H_y{}^{-}. \tag{15}$$

Definition:

$$N_\alpha^{(f,s)} = \frac{k_{z\alpha}^{(f,s)}}{n_\alpha^{(f,s)2}}, \tag{16a}$$

$$M_\alpha^{(f,s)} = -\frac{ik_{x\alpha}^{(f,s)}\varepsilon_{xz}}{n_\alpha^{(f,s)2}\varepsilon_x}. \tag{16b}$$

According to the boundary continuity condition of the electromagnetic field in the successive layers (i and j), the following is obtained:

$$\begin{bmatrix} H_j^{+} \\ H_j^{-} \end{bmatrix} = \boldsymbol{T}_j{}^{-1}\boldsymbol{T}_i\begin{bmatrix} H_i^{+} \\ H_i^{-} \end{bmatrix}, \tag{17}$$

among them.

$$\begin{aligned}\boldsymbol{T}_j{}^{-1}\boldsymbol{T}_i &= \frac{1}{2N_j}\begin{bmatrix} N_j - M_j + (N_i + M_i) & N_j - M_j - (N_i - M_i) \\ N_j + M_j - (N_i + M_i) & N_j + M_j + (N_i - M_i) \end{bmatrix} \\ &= \begin{pmatrix} \dfrac{N_i - M_i}{2N_i} & \dfrac{1}{2N_i} \\ \dfrac{N_i + M_i}{2N_i} & -\dfrac{1}{2N_i} \end{pmatrix}\begin{pmatrix} 1 & 1 \\ M_j + N_j & M_j - N_j \end{pmatrix}.\end{aligned} \tag{18}$$

Definition:

$$\boldsymbol{D}_\alpha = \begin{pmatrix} 1 & 1 \\ M_\alpha^{(f)} + N_\alpha^{(f)} & M_\alpha^{(f)} - N_\alpha^{(f)} \end{pmatrix}. \tag{19}$$

Ordinary media are not affected by magnetic fields, so $M_\alpha^{(f)} = 0$. The phase change of transmitted and reflected waves within the α layer can be expressed as:

$$\boldsymbol{P}_\alpha = \begin{pmatrix} e^{ik_\alpha^{(f)}d_\alpha} & 0 \\ 0 & e^{-ik_\alpha^{(f)}d_\alpha} \end{pmatrix}. \tag{20}$$

The total transmission matrix for FW forward and backward propagation in the NJMS can be expressed as:

$$\boldsymbol{T}_F^{(f)} = \boldsymbol{D}_0{}^{-1}\boldsymbol{N}_1\boldsymbol{N}_2\boldsymbol{N}_1\boldsymbol{N}_3\boldsymbol{N}_1\boldsymbol{D}_0, \tag{21a}$$

$$\boldsymbol{T}_B{}^{(f)} = \boldsymbol{D}_0{}^{-1}\boldsymbol{N}_4\boldsymbol{N}_3\boldsymbol{N}_4\boldsymbol{N}_2\boldsymbol{N}_4\boldsymbol{D}_0, \tag{21b}$$

where $\boldsymbol{N}_1 = (\boldsymbol{D}_2\ \boldsymbol{P}_2\ \boldsymbol{D}_2{}^{-1}\ \boldsymbol{D}_1\ \boldsymbol{P}_1\ \boldsymbol{D}_1{}^{-1})^N$, $\boldsymbol{N}_4 = (\boldsymbol{D}_1\ \boldsymbol{P}_1\ \boldsymbol{D}_1{}^{-1}\ \boldsymbol{D}_2\ \boldsymbol{P}_2\ \boldsymbol{D}_2{}^{-1})^N$, $\boldsymbol{N}_2 = \boldsymbol{D}_3\ \boldsymbol{P}_3\ \boldsymbol{D}_3{}^{-1}$, and $\boldsymbol{N}_4 = \boldsymbol{D}_4\ \boldsymbol{P}_4\ \boldsymbol{D}_4{}^{-1}$. Thus, the variation of the FW amplitude along the z-axis in the NJMS can be described as:

$$\begin{pmatrix} E_\lambda^{(f)+} \\ E_\lambda^{(f)-} \end{pmatrix} = \boldsymbol{T}^{(f)}\begin{pmatrix} E_0^{(f)+} \\ E_0^{(f)-} \end{pmatrix}. \tag{22}$$

Similarly, the relative amplitudes of the FWs of each layer in the NJMS can be derived in a similar way. The following is the derivation of the transmission matrix for the SHW. According to Maxwell's equations, the electric and magnetic fields in a nonlinear structural layer can be expressed as:[22]

$$\begin{aligned}\begin{pmatrix} E_\lambda^{(s)}(z) \\ H_\lambda^{(s)}(z) \end{pmatrix} &= \begin{pmatrix} 1 & 1 \\ N_\alpha^{(s)} & -N_\alpha^{(s)} \end{pmatrix}\begin{pmatrix} E_\lambda^{(s)+}(z) \\ E_\lambda^{(s)-}(z) \end{pmatrix} \\ &+ \begin{pmatrix} 1 & 1 \\ \dfrac{2N_\alpha^{(f)}k_f}{k_s} & -\dfrac{2N_\alpha^{(f)}k_f}{k_s} \end{pmatrix}\begin{pmatrix} A_\alpha(E_\lambda^{(f)+})^2(z) \\ A_\alpha(E_\lambda^{(f)-})^2(z) \end{pmatrix} + \begin{pmatrix} 1 \\ 0 \end{pmatrix}C_\alpha E_\lambda^{(f)+}E_\lambda^{(f)-},\end{aligned} \tag{23}$$

where $E_\lambda^{(s)+}$ and $E_\lambda^{(s)-}$ denote the amplitude of the complex electric field in the positive SHW and the negative SHW, respectively. $k_{z\alpha}^{(s)}$ and $k_{x\alpha}^{(s)}$ are the components of the wave vectors of the SHW propagating along the z-axis and the x-direction, respectively, in the medium, and satisfy $k_{z\alpha}^{(s)} = n_\alpha^{(s)}k_s\cos(X_\alpha^{(s)})$, $X_\alpha^{(s)} = \arcsin(n_0\sin\theta/n_\alpha^{(s)})$, and $k_s = 2\omega/c$, (α = 1, 2, 3, and 4). The variables A_α and C_α in the equation can be expressed as:[22]

$$A_\alpha = \frac{-4\mu\varepsilon_0\chi_\alpha^{(2)}\omega^2}{k_\alpha^{(s)2} - 4k_\alpha^{(f)2}}, \tag{24a}$$

$$C_\alpha = \frac{-4\mu\varepsilon_0\chi_\alpha^{(2)}\omega^2}{k_\alpha^{(s)2}}. \tag{24b}$$

Definition:

$$\boldsymbol{F}_\alpha = \begin{pmatrix} e^{i2k_\alpha^{(f)}d_\alpha} & 0 \\ 0 & e^{-i2k_\alpha^{(f)}d_\alpha} \end{pmatrix}, \tag{25a}$$

$$\boldsymbol{B}_\alpha = \begin{pmatrix} 1 & 1 \\ \dfrac{2N_\alpha^{(f)}k_f}{k_s} & -\dfrac{2N_\alpha^{(f)}k_f}{k_s} \end{pmatrix}, \tag{25b}$$

$$\boldsymbol{Q}_\alpha = \begin{pmatrix} e^{ik_\alpha^{(f)}d_\alpha} & 0 \\ 0 & e^{-ik_\alpha^{(f)}d_\alpha} \end{pmatrix}, \tag{25c}$$

$$\boldsymbol{G}_\alpha = \begin{pmatrix} 1 & 1 \\ M_\alpha^{(s)} + N_\alpha^{(s)} & M_\alpha^{(s)} - N_\alpha^{(s)} \end{pmatrix}. \tag{25d}$$

The expression for the output amplitude can be obtained as follows:

$$\begin{aligned}\begin{pmatrix} E_T^{(s)+}(z) \\ 0 \end{pmatrix} &= \boldsymbol{T}^{(s)}\begin{pmatrix} 0 \\ E_0^{(s)-} \end{pmatrix} + (\boldsymbol{GG}_1 + \boldsymbol{GG}_2 + \boldsymbol{GG}_3 + \boldsymbol{GG}_4 \\ &+ \boldsymbol{GG}_5),\end{aligned} \tag{26}$$

where $E_T^{(s)}$ denotes the amplitude of the SHW field transmitted from the $+z$-axis, and $E_0^{(s)}$ denotes the amplitude of the SHW field reflected from the $-z$-axis. $T^{(s)}$ is the transmission matrix of the SHW within the NJMS, and the transmission matrices of the SHW at forward incidence and backward incidence are defined as follows:

$$T_F^{(s)} = G_0{}^{-1} S_1 S_2 S_1 S_3 S_1 G_0, \quad (27a)$$

$$T_B^{(s)} = G_0{}^{-1} S_4 S_3 S_4 S_2 S_4 G_0, \quad (27b)$$

where $S_1 = (G_2\ Q_2\ G_2{}^{-1}\ G_1\ Q_1\ G_1{}^{-1})^N$, $S_4 = (G_1\ Q_1\ G_1{}^{-1}\ G_2\ Q_2\ G_2{}^{-1})^N$, $N_2 = G_3\ Q_3\ G_3{}^{-1}$, and $N_4 = G_4\ Q_4\ G_4{}^{-1}$. GG_1 to GG_5 in eqn (26) denote the effect and interference of the electric field amplitude of the individual layers of the NJMS in the FW on the amplitude of the SHW at the boundaries. $E_T^{(s)}$ and $E_0^{(s)}$ can be computed from eqn (26), and the same method can be used to obtain the SHW field in the NJMS.

Conversion efficiency is often used as a metric to describe the intensity of the SHW, and the conversion efficiency of the SHW is usually expressed as $\eta = I/I_0$, where I_0 denotes the incident light intensity and the outgoing light intensity is expressed as:[3]

$$I = \frac{1}{2} n_0 c \varepsilon_0 [(E_T^{s+})^2 + (E_0^{s-})^2]. \quad (28)$$

2.3. Principle analysis of SHW detection

Firstly, Fig. 2 shows the transmission spectra of the SHW in the NJMS with the ambient temperature fixed at 300 K. Fig. 2(a) shows the transmission spectra of SHW frequencies from 56 THz to 80 THz for EWs forward incidence, $\theta = 0°$, and we can find a clear peak of transmittance higher than 0.9 in the defect.[28] Fig. 2(b) shows the transmission spectra of EWs backward incidence, $\theta = 85°$, with SHW frequencies from 50 THz to 75 THz. We can similarly find that there is a clear peak of transmittance higher than 0.9 in the defects.[28] The frequency points of the peaks within the defect band correspond to strong resonance points, which are easier to detect. It can also be found that the peaks at forward and backward incidence appear at different frequencies, showing the Janus characteristic, which provides the possibility of realizing the function of different modes and detection ranges in the forward and backward directions.

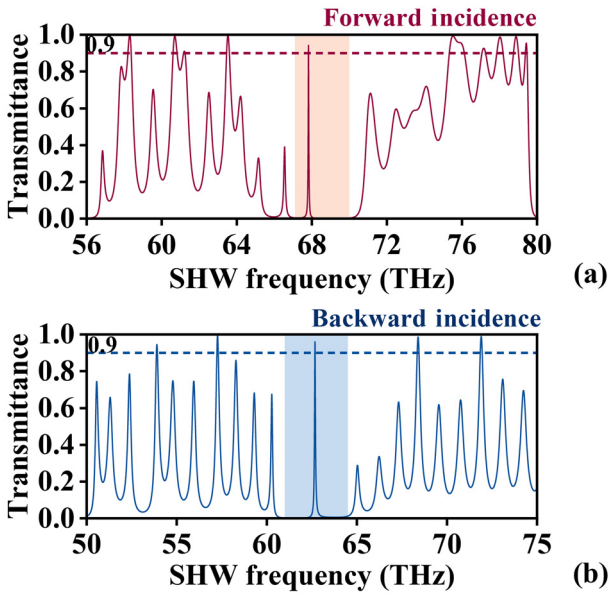

Fig. 2 Transmission spectra of the SHW in the NJMS. (a) Transmission spectra of SHW frequencies from 56 THz to 80 THz for EWs forward incidence with $\theta = 0°$, and (b) transmission spectra of SHW frequencies from 50 THz to 75 THz for EWs backward incidence with $\theta = 85°$.

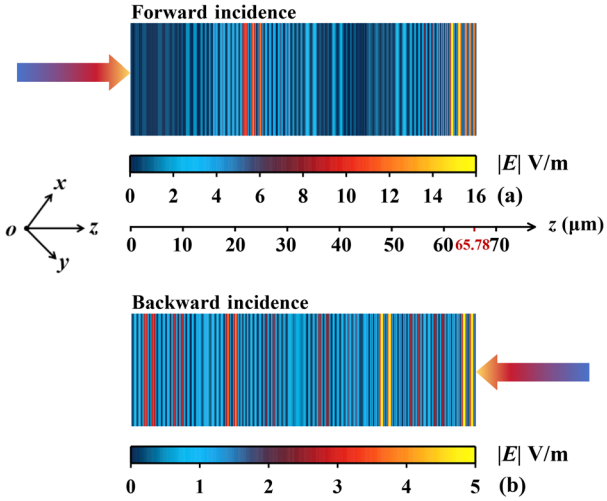

Fig. 3 E-Field distribution of the NJMS along the + z direction. (a) E-Field distribution of the NJMS at SHW frequency f = 67.82 THz for EWs forward incidence, $\theta = 0°$. (b) E-Field distribution of the NJMS at SHW frequency f = 62.67 THz for EWs backward incidence, $\theta = 85°$.

To explain more specifically why the peak appears, Fig. 3 shows the electric field distribution of the NJMS along the +z direction at the frequency point where the peak occurs in Fig. 2. Fig. 3(a) shows the electric field distribution of the NJMS at the forward incidence of EWs, $\theta = 0°$, and at the SHW frequency f = 67.82 THz, and we can find that the energy occurs in the localized domain. Fig. 3(b) shows the electric field distribution of the NJMS at EWs backward incidence, $\theta = 85°$, and at the SHW frequency f = 62.67 THz, and we can similarly find that the energy has undergone localization.

Fig. 4 demonstrates the specific frequency point at which the peak transmittance under the SHW occurs and the conversion efficiency at that frequency point at a fixed ambient temperature of 300 K and an incident light intensity I_0 = 0.1 GW cm^{-2}. We should select a high-power THz source, operating within the frequency range of 0.1 THz to 675 THz, as the laser source. This laser source is renowned for its high peak power and low single-pulse energy, making it an ideal light source for the effect of SHW generation.[29] As shown in Fig. 4(a) and (b), when the SHW frequency f = 67.82 THz, the EWs are incident forward, $\theta = 0°$, and the SHW output efficiency reaches 60.98%. When the SHW frequency f = 62.67 THz, the EWs are incident backward, $\theta = 85°$, and the SHW output efficiency reaches 1627%. Hulme *et al.* demonstrated SHW generation of blue light on an integrated thin-film lithium niobate waveguide and observed a conversion efficiency of 33 000%.[30] Compared with the experimental results of Li *et al.*,[23] which required a light intensity as high as 0.5 GW cm^{-2} to obtain a

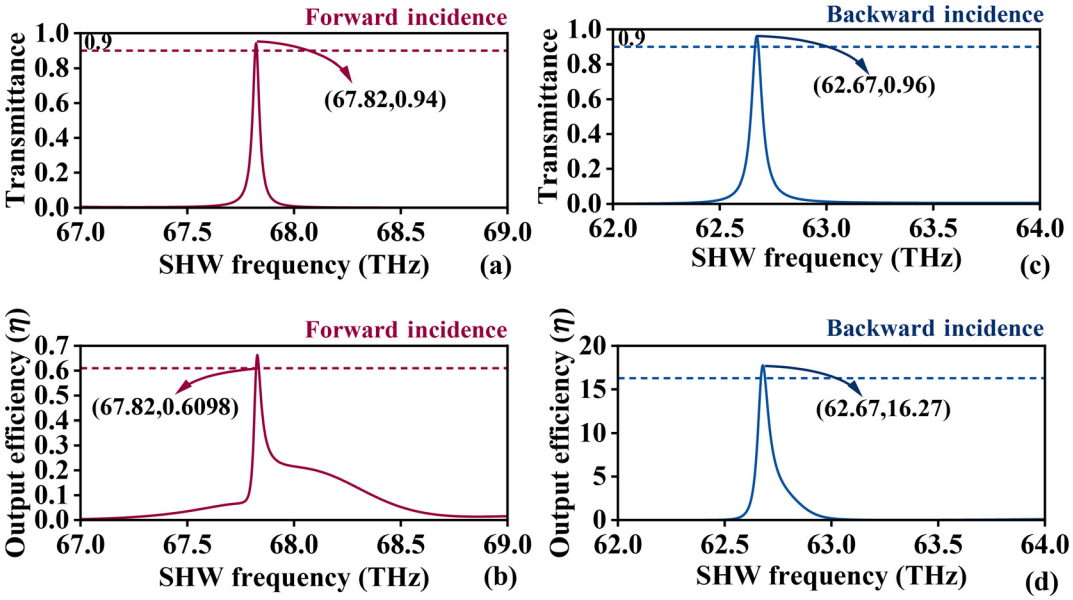

Fig. 4 Specific frequency points at which the peak transmittance occurs under the SHW and the conversion efficiency at that frequency point. (a and b) Specific frequency points at which the peak transmittance occurs under the SHW at forward incidence of EWs, θ = 0°, and the conversion efficiency at that frequency point. (c and d) Specific frequency points at which the peak transmittance occurs under the SHW at backward incidence of EWs, θ = 85°, and the conversion efficiency at that frequency point.

significant conversion efficiency, the output intensity in this paper exhibits higher efficiency and lower energy consumption. Therefore, in this paper, by changing the angle θ and detecting the RI of the layer and the thickness of the layer of several physical quantities, it is found that the frequency point where the peak value of the transmittance is located is regularly shifted and shows different patterns in the forward and backward directions, and the design of the NJMS based on the detection of the second harmonic of the multi-physical quantities is proposed.

3. Discussion of parameters

In this paper, the NJMS is proposed for detecting RI, thickness, and angle θ with the Janus property. The detection function is realized using peak transmission frequency (PTF) variation with physical quantities. This provides a new idea for the study of multi-physical quantity detection and Janus detection. The following discusses three physical quantities: RI, thickness, and angle θ, respectively. Finally, the research results are compared with those of the existing ones to present the superiority and limitations of the NJMS. To evaluate the detection performance of the NJMS, several important globally harmonized evaluation parameters are introduced, including sensitivity (S) and quality factor (Q). The relevant formulas for the calculation of these parameters are given below:[31]

$$S = \frac{\Delta f}{\Delta x}, \tag{29a}$$

$$Q = \frac{f_T}{\mathrm{FWHM}}. \tag{29b}$$

In eqn (29), Δx and Δf denote the increment of the measured physical quantity and the associated change in the PTF of the SHW, respectively. The PTF of the SHW and its half-maximum full width are denoted by f_T and half-height full width (FWHM), respectively. A perfect sensor should have a higher sensitivity, Q, value, which indicates a more sensitive PTF response.[31] In addition, the higher the Q value, the higher the sensitivity.[31]

Fig. 5 presents the transmission spectra of different period numbers N = 1, 2, 3, 4, 5, and 6. Through the discussion on

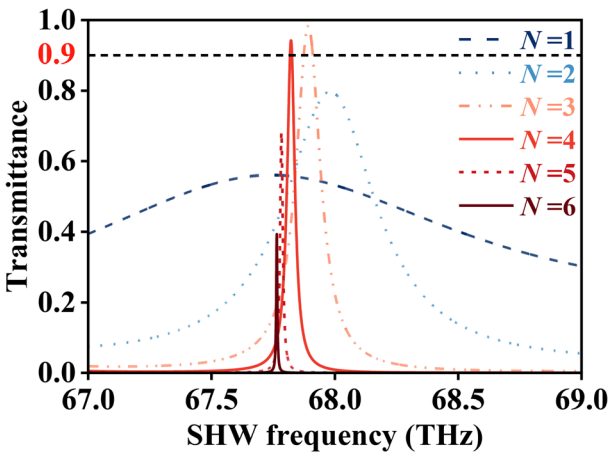

Fig. 5 Transmittance spectra for different numbers of periods N = 1, 2, 3, 4, 5, and 6 in the NJMS.

the number of periods, we can conclude that as the number of cycles increases, the Q value of the transmission peak continues to rise. However, since the transmission peak values exceed 0.9 only when $N = 3$ and $N = 4$, the one with a higher Q value between the two is selected as the value of N.

3.1. RI detection

This paper provides insight into the ability of the NJMS to measure the RI (n_4) under specific environmental conditions accurately. Specifically, the study focuses on the performance of the NJMS in detecting the RI (n_4) of the detection layer (P_4) in the interval of 1.80 to 2.00 when the ambient temperature T is kept constant at 300 K, the applied magnetic field strength B is set at 1 T, $d_4 = 1.45$ μm, and the forward incidence angle θ is fixed at 85°.

Fig. 6(a) demonstrates the complex relationship between n_4 and SHW frequency and transmittance under the above conditions in an intuitive three-dimensional graphical manner, clearly revealing that the PTF exhibits a significant linear trend as n_4 varies within the specified range. This finding provides a solid data basis for evaluating the detection efficacy of the NJMS. To quantify the detection accuracy of the NJMS, linear regression analysis with a coefficient of determination R^2 is introduced as an evaluation tool in this study. The value of R^2 tends to be 1, which signifies superior detection performance.[31] R^2 greater than or equal to 0.99 is often regarded as a threshold mark for high detection accuracy.[31] As shown in Fig. 6(b), the results demonstrate a highly linear correlation by selecting reference points at 0.05 and linearly fitting n_4 to the PTF. The functional relationship can be expressed as $f = -1.4309n_4 + 63.5249$ (THz). Thus, the S of the NJMS for n_4 detection is calculated to be −1.4309 THz RIU^{-1} with a high R^2 of 0.9929, fully confirming its excellent detection performance. Furthermore, Fig. 6(c) reveals that the NJMS can reach a maximum Q value of 932.1 during detection. In contrast, the minimum value remains at a high level of 750.9, demonstrating its potential for high-resolution detection by constructing a three-dimensional plot of the relationship between n_4, the SHW frequency, and the Q value. Fig. 6(d) focuses on the detailed analysis of the SHW transmission property concerning the variation of n_4, and the transmission curves are plotted for different values of n_4 utilizing reference points selected at 0.05 intervals along the +x-axis. These curves clearly demonstrate the significant shift of the PTF over the range of n_4 variations, which not only verifies the sensitive response of the NJMS to RI changes but also highlights its excellent performance in detection accuracy and stability. Notably, the unique pattern changes in the transmission spectra when EWs are applied to the system in a backward incidence mode. This opens up new perspectives for exploring the performance of the NJMS under different incidence conditions and foretells the broad application of this technology in the field of complex optical inspection.

Fig. 7 demonstrates the accurate detection capability of the NJMS for the RI (n_4) of the detection layer P_4 over a wide range of 1.40 to 1.90 for an incidence angle of 85° backward, where

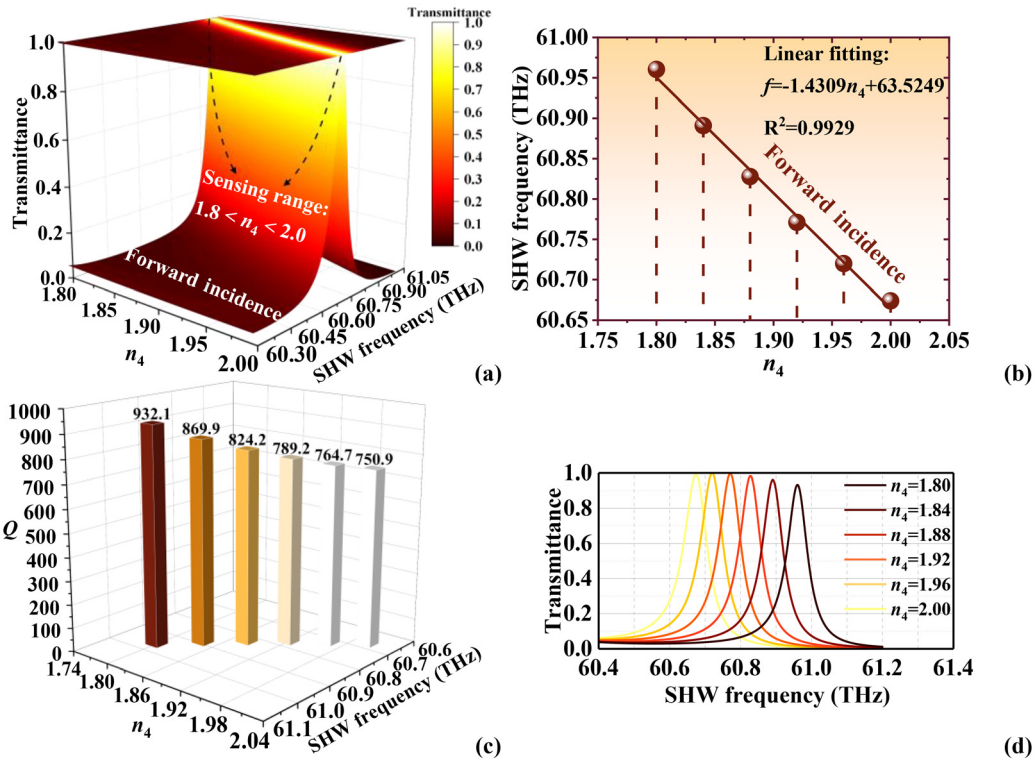

Fig. 6 Detection of the RI by the forward-incident SHW. (a) Changing PTF. (b) Linear relationship between n_4 and SHW frequency. (c) Q values at different PTFs. (d) Transmission spectra at different n_4 values.

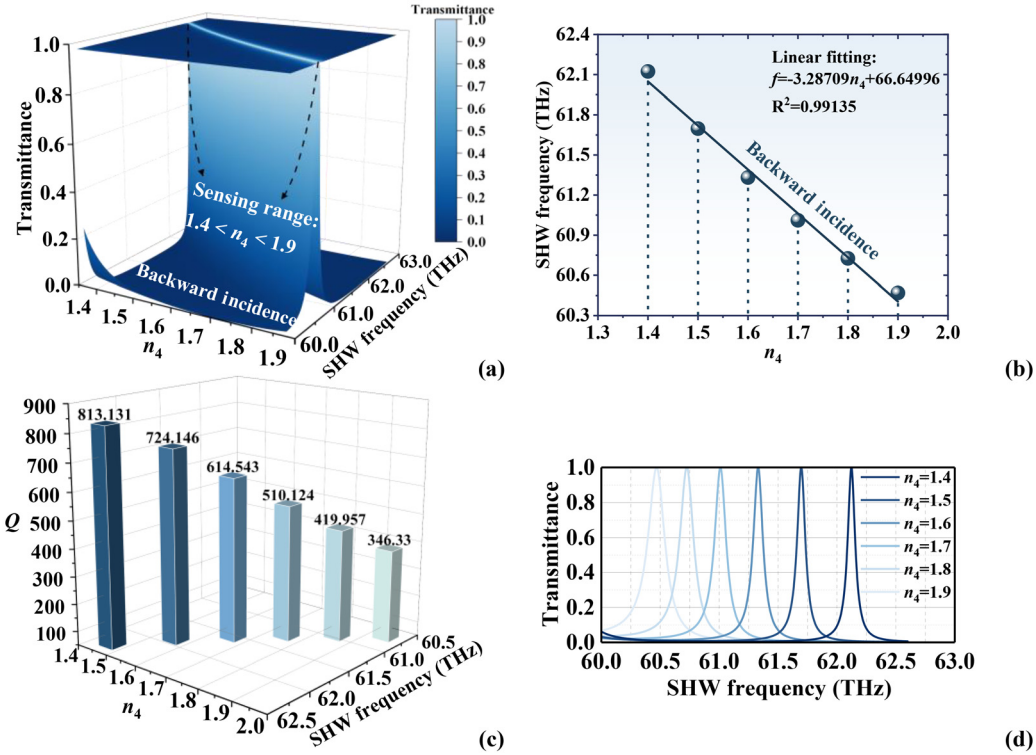

Fig. 7 Detection of the RI by the backward-incident SHW. (a) Changing PTF. (b) Linear relationship between n_4 and SHW frequency. (c) Q values at different PTFs. (d) Transmission spectra at different n_4 values.

the reference point is selected with an accuracy of 0.1. In Fig. 7(a), the lower limit of the detection range is up to 1.44. In Fig. 7(b), the fitted function is given as $f = -3.28709n_4 + 66.64996$ (THz), the sensitivity $S = -3.28709$ THz RIU^{-1}, and $R^2 = 0.99135$. In Fig. 7(c), the highest Q value soars to 813.131 while the lowest remains at a high level of 346.33, emphasizing the high resolution detection capability of the system. Fig. 7(d) also verifies the sensitive response of the NJMS to RI changes. Compared with the forward-incidence configuration, the backward-incidence configuration broadens the detection range and significantly improves the sensitivity, reflecting the innovation and optimization of the detection strategy.

3.2. Thickness detection

Fig. 8 provides an insight into the ability of the NJMS to accurately monitor the thickness d_4 of P_4 in the fine interval from 1.35 μm to 1.47 μm under specific conditions with a forward incidence angle of 0°, where the reference point is selected with an accuracy of 0.02 μm, and at this time, the RI of P_4 is set to be $n_4 = 1.28$. By constructing the three-dimensional plots of the relationship between d_4, the SHW frequency, and transmittance in Fig. 8(a), the linear relationship between d_4 and PTF, $f = -0.5979d_4 + 68.6890$ (THz), $S = -0.5979$ THz μm^{-1}, and $R^2 = 0.9936$ are obtained in Fig. 8(b). The highest Q value in Fig. 8(c) jumps to 2030.3, while the lowest value is also kept at 1528.9. Fig. 8(d) visualizes the significant shift phenomenon of the PTF, which proves the excellent detection performance of the NJMS.

Fig. 9 shows the accurate monitoring capability of d_4 in the narrow interval of 1.45 μm to 1.50 μm under the condition of changing the incidence angle set to 85° backward, where the reference point is still selected with an accuracy of 0.02 μm. In Fig. 9(a), compared with forward incidence, this configuration not only adjusts the boundary of the detection range but successfully extends the lower detection limit to 1.35 μm while maintaining a high degree of sensitivity to d_4 variations. In Fig. 9(b), the fitted function is $f = -1.9714d_4 + 65.6102$ (THz), $S = -1.9714$ THz μm^{-1}, and $R^2 = 0.9997$, with a significant increase in the sensitivity value, highlighting the advantages of the backward-incidence configuration for specific detection tasks. Fig. 9(c) and (d) reveal the high stability of the Q value and the significant offset phenomenon of the PTF during the detection process.

3.3. Angle detection

In Fig. 10, the slight variation of the angle θ in the range of 14° to 19° at forward incidence was detected under the conditions of $d_4 = 1.45$ μm and $n_4 = 1.28$ of P_4, in which the reference point was selected with an accuracy of 1°. In Fig. 10(a) and (b), the relationship between θ and PTF is fitted for $f = -0.0736\theta + 67.2167$ (THz), $S = -0.0736$ THz per °, $R^2 = 0.9979$. The Q value remains at a high level up to 1496.8 and as low as 1180.6 in Fig. 10(c). In Fig. 10(d), the performance of the NJMS in accurately capturing the angular variations is verified.

Fig. 11 demonstrates the detection of θ in the range of 80° to 85° at backward incidence. Fig. 11(a) and (b) depict that as θ

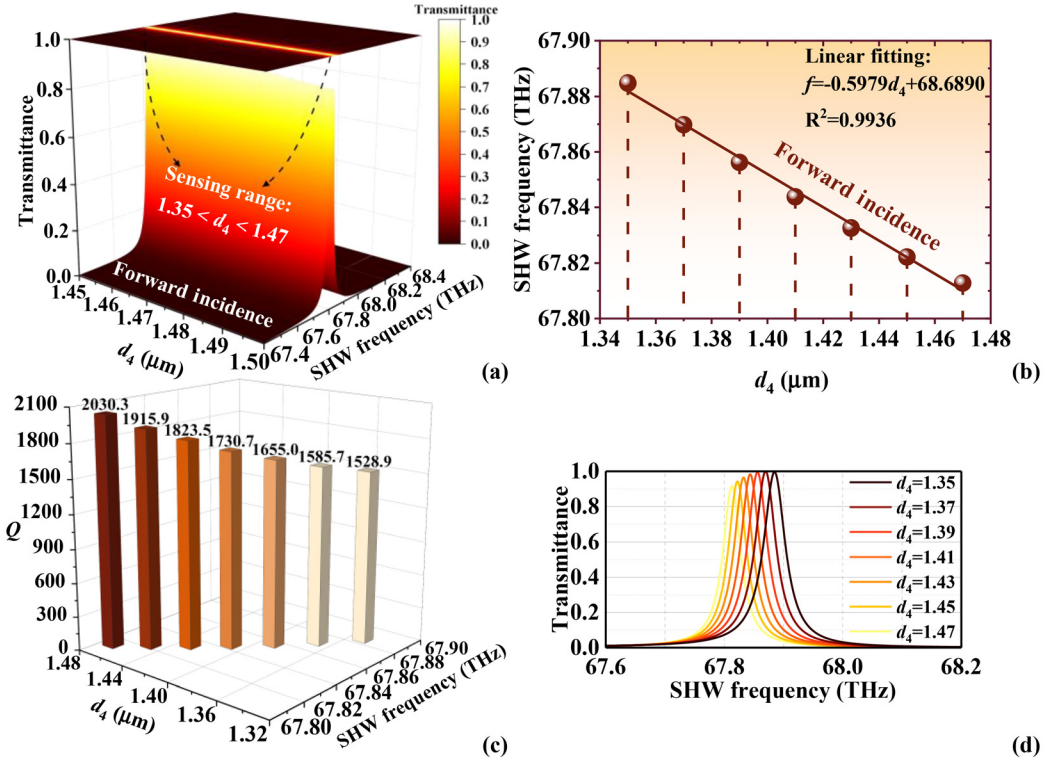

Fig. 8 Detection of thickness by the forward-incident SHW. (a) Changing PTF. (b) Linear relationship between d_4 and SHW frequency. (c) Q values at different PTFs. (d) Transmission spectra at different d_4 values.

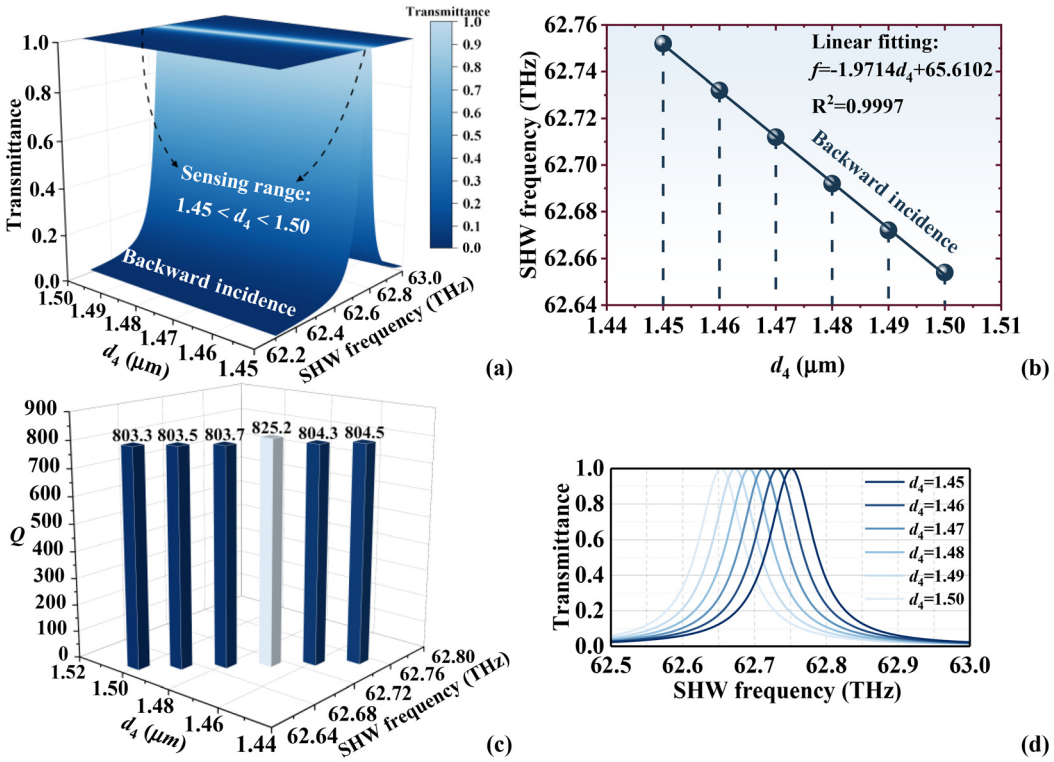

Fig. 9 Detection of thickness by the backward-incident SHW. (a) Changing PTF. (b) Linear relationship between d_4 and SHW frequency. (c) Q values at different PTFs. (d) Transmission spectra at different d_4 values.

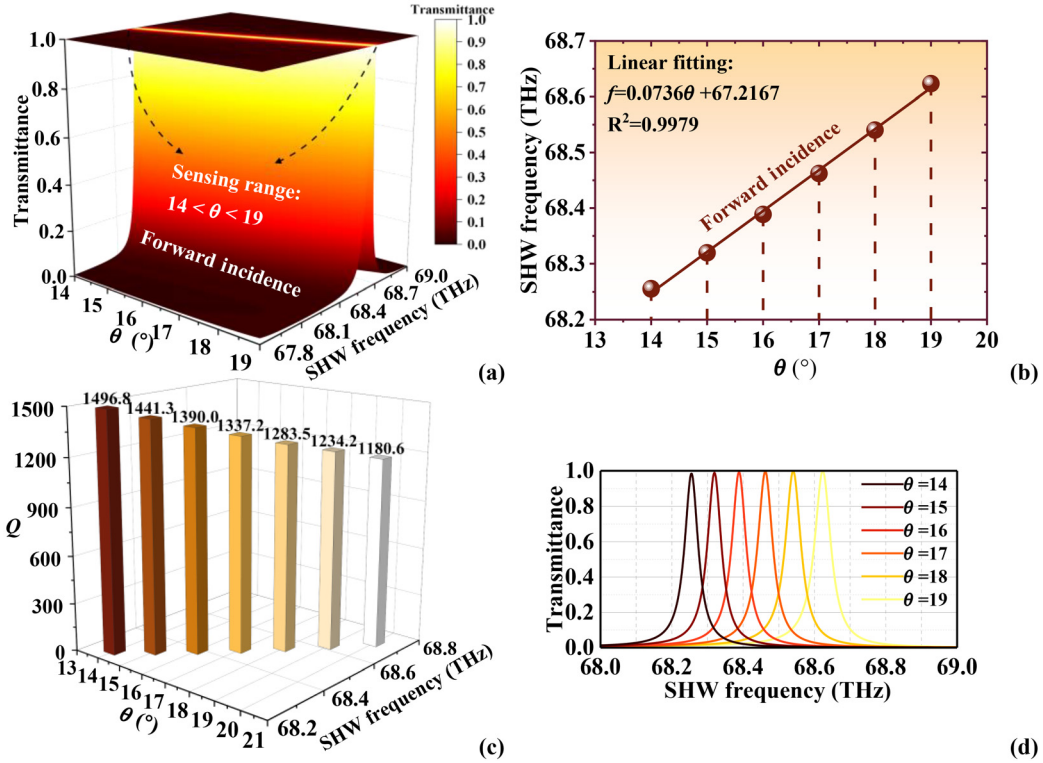

Fig. 10 Detection of angle by the forward-incident SHW. (a) Changing PTF. (b) Linear relationship between θ and SHW frequency. (c) Q values at different PTFs. (d) Transmission spectra at different θ values.

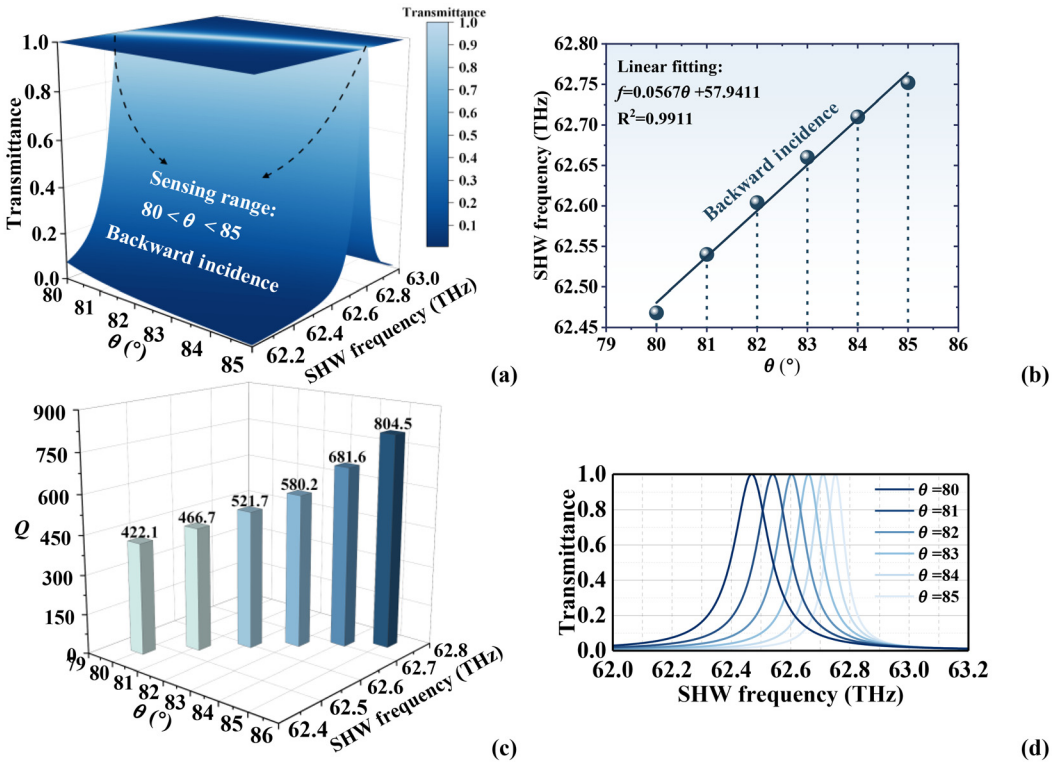

Fig. 11 Detection of angle by the backward-incident SHW. (a) Changing PTF. (b) Linear relationship between θ and SHW frequency. (c) Q values at different PTFs. (d) Transmission spectra at different θ values.

varies in the range from 80° to 85, the PTF shows a linear variation of $f = -0.0567n_4 + 57.9411$ (THz), with $S = -0.0567$ THz per °, and $R^2 = 0.9911$, presenting different sensitivities compared to the forward incidence, which is lower than that of the forward incidence. In Fig. 11(c), it can be found that the maximum Q value of detection can reach 804.5 and the minimum is 422.1. The obvious shift of the PTF in Fig. 11(d) demonstrates the perfect detection performance of the NJMS.

The selection of the incidence angle θ during the detection process is a result of overall consideration. For the backward incidence setup, after comprehensively evaluating the transmission peak, Q value, sensing range, and sensitivity, we found that setting the incidence angle to 85° for both forward and backward sensing of the refractive index yields optimal results. To enhance the practicality and maneuverability of the design, we continue to adopt the backward incidence angle of 85° for thickness measurement. However, in forward thickness detection, since there is no transmission peak at 85° incidence, detection cannot be performed. Conversely, at 0° incidence, better sensing performance is achieved; thus we set the forward incidence angle to 0°. While these incidence angle selections may not be optimal for the measurement of a single physical quantity, they are more suitable for multi-physical quantity detection.

Table 1 The multi-physical quantity detection performance of the NJMS

Physical quantity	Detection range		Maximum value of Q	Total range
n_4	Forward	1.80–2.00	932.1	1.40–2.00
	Backward	1.40–1.90	813.1	
d_4	Forward	1.35–1.47 μm	2030.3	1.35–1.50 μm
	Backward	1.45–1.50 μm	825.2	
θ	Forward	14–19°	1496.8	14–19° and
	Backward	80–85°	804.5	80–85°

To show the detection performance of the NJMS more clearly, Table 1 summarizes the detection range of each detection index of the NJMS.

3.4. Comparison of relevant studies

Finally, to compare the proposed NJMS with designs in related fields, this paper summarizes the recent applications of the SHW in the field of RI, thickness, and angle θ detection, as shown in Table 2.[32–35] There are relatively SHW-based detectors in the field of physical quantity detection. Therefore, the research on the simultaneous realization of SHW detection is highly innovative, indicating considerable potential to be explored in this direction. In addition, as shown in Table 2, most of the previous studies lacked the Janus functionality, thus limiting its application scope and flexibility. In contrast, the proposed NJMS improves the sensitivity and extends the measurement range through SHG. Notably, the NJMS resolves the limitations of conventional detectors in multifunctional integration and realizes the detection of the SHW with the Janus feature, which is a precious achievement. In addition, the Q value of the NJMS is generally high, which is of great value in fields requiring high-resolution detection. For the realization of RI, thickness, and angle θ detection in different modes in the forward and backward directions, the NJMS is a significant advancement with remarkable innovation and versatility.

4. Conclusion

In conclusion, an innovative NJMS design consisting of SBN, magnetized InSb, and a common medium is presented. The RI, thickness, and angle θ detection is realized by employing the SHW and Janus properties to expand the detection range and application scenarios effectively. Compared with previous

Table 2 Comparison of published studies with the proposed NJMS in terms of performance

Ref.	SHW	Multi-physics	Janus	Detection physical quantities		Detection performance	
32	√	×	×	Angle detection		Range	51.5°–54.5°
						S	0.00314 nm per arcs
33	×	×	×	Waterborne bacteria detection		Range	1.333–1.422
						S	387.5 nm RIU^{-1}
34	×	×	×	RI detection		Range	1.42–1.54
						S	11 700 nm RIU^{-1}
35	×	×	×	RI detection		Range	1.3323–1.3561
						S	677 nm RIU^{-1}
This work	√	√	√	RI detection	Forward	Range	1.80–2.00
						S	1.4309 THz RIU^{-1}
					Backward	Range	1.40–1.90
						S	3.28709 THz RIU^{-1}
				Thickness detection	Forward	Range	1.35–1.47μm
						S	0.5979 THz μm^{-1}
					Backward	Range	1.45–1.50 μm
						S	1.9714 THz μm^{-1}
				Angle detection	Forward	Range	14–19°
						S	0.0736 THz per °
					Backward	Range	80–85°
						S	0.0567 THz per °

studies, the NJMS focuses on electromagnetic devices that realize multi-physical quantity detection and multi-application scenarios, demonstrating a more promising and innovative detection method. This design provides a new approach for multi-physical quantity detection, nonlinear optics research, and improving detector performance in different scenarios. It has great potential in several areas, such as multifunctional device design and SHW applications.

Author contributions

Yu-Xin Wei: writing – original draft, investigation, data curation, methodology, and conceptualization. Jun-Yang Sui: writing – review & editing, visualization, supervision, methodology, and conceptualization. Chuan-Qi Wu: visualization and conceptualization. Chu-Ming Guo: supervision, methodology, and conceptualization. Xiang Li: visualization, supervision, methodology, and conceptualization. Hai-Feng Zhang: writing – review & editing, supervision, and conceptualization.

Data availability

The data that support the findings of this study are available from the corresponding author upon reasonable request.

Conflicts of interest

The authors declare no conflict of interest.

Acknowledgements

This work was supported by the National College Students Innovation and Entrepreneurship Training Program (Grant No. 202410293018Z), and the College Student Innovation Training Program of Nanjing University of Posts and Telecommunications.

References

1 V. A. Makarov, *Kvantovaya Elektron.*, 2011, **41**, 957.
2 S. Z. Zhang, X. B. Li, Y. O. Jeong and S. O. Cho, *IEEE Trans. Instrum. Meas.*, 2019, **68**, 3635–3646.
3 C. Yang, C. M. Guo, C. Peng and H. F. Zhang, *Ann. Phys.*, 2023, **535**, 2300190.
4 X. Y. Li, Q. Wei, C. L. Hu, J. Pan, B. X. Li, Z. Z. Xue, X. Y. Li, J. H. Li, J. G. Mao and G. M. Wang, *Adv. Funct. Mater.*, 2023, **33**, 2210718.
5 J. Martorell, R. Vilaseca and R. Corbalán, *Appl. Phys. Lett.*, 1997, **70**, 702–704.
6 A. Bahabad, M. M. Murnane and H. C. Kapteyn, *Nat. Photonics*, 2010, **4**, 570–575.
7 S. N. Nihtianov, G. P. Shterev, N. Petrov and G. C. M. Meijer, *IEEE Trans. Instrum. Meas.*, 2001, **50**, 976–980.
8 J. Liu, C. Ouyang, F. Huo, W. He and A. Cao, *Dyes Pigm.*, 2020, **181**, 108509.
9 E. E. M. Khaled, S. C. Hill and P. W. Barber, *Appl. Opt.*, 1994, **33**, 3308–3314.
10 A. Fiore, V. Berger, E. Rosencher, P. Bravetti and J. Nagle, *Nature*, 1998, **391**, 463–466.
11 S. Zhu, Y. Y. Zhu and N. B. Ming, *Science*, 1997, **278**, 843–846.
12 F. Conversano, A. Greco, E. Casciaro, A. Ragusa, A. Lay-Ekuakille and S. Casciaro, *IEEE Trans. Instrum. Meas.*, 2012, **61**, 1848–1856.
13 T. Wada, J. Nakazoe and Z. Abe, *IEEE Trans. Instrum. Meas.*, 1977, **26**, 377–383.
14 W. Dwi Astuti, H. Matsukuma, M. Nakao, K. Li, Y. Shimizu and W. Gao, *Sensors*, 2021, **21**, 670.
15 S. Iida, O. Ishii and S. Kambe, *Jpn. J. Appl. Phys., Part 2*, 1998, **37**, L869–L871.
16 D. L. Sounas and A. Alù, *Nat. Photonics*, 2017, **11**, 774–783.
17 A. E. Omer, A. Hojjati-Firoozabadi, S. Gigoyan, S. Safavi-Naeini and G. Shaker, *IEEE Trans. Instrum. Meas.*, 2022, **71**, 1–12.
18 A. S. Kewitsch, T. W. Towe, G. J. Salamo, A. Yariv, M. Zhang, M. Segev, E. J. Sharp and R. R. Neurgaonkar, *Appl. Phys. Lett.*, 1995, **66**, 1865–1867.
19 A. S. Kewitsch, T. W. Towe and G. J. Salamo, *Appl. Phys. Lett.*, 1995, **66**, 1865–1867.
20 K. F. Hulme and J. B. Mullin, *Solid-State Electron.*, 1962, **5**, 211-IN10.
21 S. Guo, C. Hu and H. Zhang, *J. Opt.*, 2020, **22**, 105101.
22 L. Qi, Z. Yang, F. Lan, X. Gao and Z. Shi, *Phys. Plasmas*, 2010, **17**, 042501.
23 J. Li, Z. Li, Y. Sheng and D. Zhang, *Appl. Phys. Lett.*, 2007, **91**, 022903.
24 F. Fan, S.-J. Chang, W.-H. Gu, X.-H. Wang and A.-Q. Chen, *IEEE Photonics Technol. Lett.*, 2012, **24**, 2080–2083.
25 P. P. Trokhimchuck, *IEEE Xplore*, 2008, **7009**, 700906–700901.
26 J.-Y. Sui, J.-H. Zou, S.-Y. Liao, B.-X. Li and H.-F. Zhang, *Appl. Phys. Lett.*, 2023, **122**, 231105.
27 Y. T. Fang, L. Han and Y. F. Gao, *Z. Naturforsch., A: Phys. Sci.*, 2015, **70**, 205–211.
28 J.-J. Li, Z.-Y. Li and D.-Z. Zhang, *Phys. Rev. E:Stat., Nonlinear, Soft Matter Phys.*, 2007, **75**, 056606.
29 O. Schubert, M. Hohenleutner, F. Langer, B. Urbanek, C. Lange, U. Huttner, D. Golde, T. Meier, M. Kira, S. W. Koch and R. Huber, *Nat. Photonics*, 2014, **8**, 119–123.
30 T. Park, H. S. Stokowski, V. Ansari, T. P. McKenna, A. Y. Hwang, M. Fejer and A. H. Safavi-Naeini, *Opt. Lett.*, 2022, **47**, 2706–2709.
31 Z. A. Zaky, A. M. Ahmed, A. S. Shalaby and A. H. Aly, *Sci. Rep.*, 2020, **10**, 9736.

32 W. D. Astuti, K. Y. Li, R. Sato, H. Matsukuma, Y. Shimizu and W. Gao, *Appl. Sci.*, 2022, **12**, 5211.
33 A. Panda and P. D. Pukhrambam, *Phys. B*, 2021, **607**, 412854.
34 A. K. Paul, M. S. Habib, N. H. Hai and S. A. Razzak, *Opt. Commun.*, 2020, **464**, 125556.
35 S. Ghorbani, M. Sadeghi and Z. Adelpour, *Laser Phys.*, 2019, **30**, 026204.